공학석사 학위논문

Convolutional Neural Network based Pore Detection using the Melt Pool Monitoring Data in the Selective Laser Melting Additive Manufacturing Process

선택적 레이저 용융 적층 제조 공정의 용융풀 데이터를 활용한 합성곱 신경망 기반 기공 감지

2022 년 2 월

서울대학교 대학원

항공우주공학과

이 한 울

Convolutional Neural Network based Pore Detection using the Melt Pool Monitoring Data in the Selective Laser Melting Additive Manufacturing Process

선택적 레이저 용융 적층 제조 공정의 용융풀 데이터를 활용한 합성곱 신경망 기반 기공 감지

지도 교수 윤 군 진

이 논문을 공학석사 학위논문으로 제출함

2022 년 2 월

서울대학교 대학원

항공우주공학과

이 한 울

이한울의 공학석사 학위논문을 인준함

2022 년 2 월

위 원 장 김 도 년 (인)

부위원장 윤 군 진 (인)

위 원 이 호 원 (인)

Abstract

Convolutional Neural Network based Pore Detection using the Melt Pool Monitoring Data in the Selective Laser Melting Additive Manufacturing Process

Han Wool Lee
Department of Aerospace Engineering
The Graduate School
Seoul National University

This thesis is about a method for detecting the internal pores in the additive manufacturing (AM) process, especially selective laser melting (SLM). Metal additive manufacturing has the advantage of producing parts with complex shapes more easily and quickly than traditional manufacturing methods (cutting, casting, etc.). As this gradually expanded, non-destructive inspection methods using X-rays have been mainly used to ensure the quality of parts, but they have the disadvantage of being costly and time-consuming. To overcome such limitations, several methods using various data (images, acoustic signals, etc.) in artificial intelligence have been attempted. In this

thesis, defects caused by lack-of-fusion and keyholes pores are predicted through a three-dimensional convolutional neural network (3D-CNN) based on photodiode light intensity data reflected from the melt pool during the process. Specimens with artificial defects are manufactured by arbitrarily setting the energy density from 19.84 J/mm^3 to 110.12 J/mm^3, as a process parameter. The proposed network takes the three-dimensional light intensity data collected during the process as an input, scans it with a small 3D moving window performing local inspection, and is trained by matching the output value labeled with the micro-CT results. In order to predict the type of pores and the local volume fraction as output values, a joint model is used which classification and regression are calculated simultaneously. Furthermore, test specimens with random pores are fabricated to evaluate the performance. As a result, the proposed model can detect pores with a diameter over 80 μm with a true positive ratio of up to 78.37% in both lack-of-fusion and keyhole cases.

Keywords : Additive Manufacturing, Selective Laser Melting, Convolutional Neural Network, Melt Pool Monitoring, Defect Detection

Student Number : 2020-26197

Table of contents

List of figures

List of tables

1. Introduction

1.1. Motivation

Recently, 3D printing, in which materials from the bottom to the top are stacked in continuous layers, is attracting attention as a new-generation production technology. Especially in the aviation industry, the manufacture of aviation parts utilizing additive manufacturing tends to expand due to various advantages such as structural, electrical, and electronic parts. Since the degree of freedom in shape is higher than that of casting and cutting, which are traditional manufacturing methods, it is easy to remove unnecessary parts with the same physical characteristics. It has been applied to various components due to the advantages of reducing overall airframe weight, improving fuel efficiency, and increasing range [1]. However, since it is necessary to meet high-quality requirements, additional examinations (e.g. CT scans) are required for quality inspection of parts manufactured through additive manufacturing. Moreover, it is not easy to apply to all printed parts because of part size and production costs [2].

In particular, due to the spot diameter of less than 100um and the

high laser power input of this method, a large temperature gradient is formed and residual stress and deformation of the part are formed inside the part [3, 4]. The porosity is a typical defect in the process and negatively affects the mechanical properties of the manufactured parts. The pores generated in the PBF process are appeared in various forms and are generally classified by lack-of-fusion, keyhole mode melting. Melt pool dynamics, a complex physical mechanism involving partial material melting and vaporization, cause the formation of these pores [5, 6]. The cause and defects are various (e.g., thermal history, residual stress, and grain in microstructure), but pore detection is highlighted in this thesis due to their effect on mechanical properties like fatigue behavior [7].

In some additive manufacturing equipment, the amount of light reflected by the input laser while melting the material is stored via a photodiode in a data format known as melt pool monitoring (MPM) data. The MPM data includes the position (Cartesian coordinates) and the amount of light at the moment when the laser is irradiated, and when the laser frequency is 60 kHz, it stores the number of 60,000 data per second, so it is possible to acquire data at very detailed positions.

Additional algorithms are required, but using these data, it is easy to identify specific points that are significantly higher or lower in the average laser light intensity, and defects can be detected by correlating with the porosity occurring in that area [8]. Therefore, this thesis proposes a new method that uses artificial intelligence to predict the location, size, and overall volume fraction of pores using only MPM data by correlating the collected data with the real pores detected through actual micro-CT scanning.

2. Backgrounds and related researches

2.1. Theoretical background

2.1.1. Metal additive manufacturing

Typically, additive manufacturing methods for producing metal products are divided into powder bed fusion (PBF) and direct energy deposition (DED). These two are distinguished by the difference in the method of supplying powder and sintering with a laser. PBF is a method in which a metal powder of a specific area is evenly distributed

in a separate powder supply device and then only a desired part is selectively irradiated with a laser to sinter. DED is a method in which powder is supplied in real-time through a nozzle and melted immediately with a high-power laser for lamination [9, 10]. PBF type additive manufacturing equipment is advantageous for implementing the degree of freedom of shape and is adopted by many companies including EOS GmbH.

The selective laser melting (SLM) process, which is one of the PBF methods, is shown in Figure 1. A powder supply device spreads a thin spherical metal powder on the build plate or previous layer, and melts only the required parts using a high-power laser. In the sintered part, the metal is solidified, Heat is transferred more quickly than in the powder state, and heat is passed through the build plate. The photodiode collects the instantaneous amount of reflected laser light and stores it in chronological order [10]. In this study, M290 printer and melt pool analyzing software of EOS are used, and the stored data can be displayed in real-time and analyzed according to the algorithm provided by the equipment manufacturer. However, since data are displayed for each layer, there is a limitation to evaluate overall quality

of parts at a glance.

2.1.2. Melt pool monitoring system

The melt pool means a part where the base metal portion melted by the arc heat is dented during welding of the original metal. Since the PBF method also melts the powder with a heat source, a melt pool is formed in the same way. The shape of the melt pool changes depending on the amount of energy input to the metal powder material. If excessive energy is input per unit area, the depth of the melt pool becomes deeper (called a keyhole welding), and conversely, if low energy is applied, the depth of the melt pool becomes shallow (called conduction welding) [11]. In the former case, the material is vaporized to cause voids in the melt pool, and in the latter case, the powder cannot be completely melted and remains in the powder state, weakening the bond with the surrounding layer [12]. Therefore, it is possible to indirectly determine whether or not appropriate energy is input to melt material through the amount of reflected light.

As shown in Figure 1, In the case of EOS melt pool monitoring equipment, melt pool intensity, scanner position, laser trigger (on/off),

and exposure type (e.g., inskin, contour, etc.) are stored at 60kHz frequency. Dedicated software visualizes this and analyzes melt pool intensity according to three algorithms (absolute limits, signal dynamics, short term fluctuations) to estimate defects by providing an indication when the signal exceeds a user-specified threshold [8]. The user can find out whether a defect exists by adjusting the threshold or sensitivity, but the location of the defect cannot be estimated. Furthermore, since the original data cannot be edited, it is impossible to determine whether a defect has been created completely. Therefore, there is a need to detect defects by analyzing the original data in another method without using the corresponding software. In this thesis, the original data is reversely extracted from the software and then used as base data. However, since the layer thickness is very minimal (about 30~40um) and the amount of data of each layer is large, the overall data size is enormous per one specimen. For example, a specimen with 10mm height creates about 250 to 333 data files and the data capacity is about 50GB. To process this data, an appropriate algorithm considering computational power is needed.

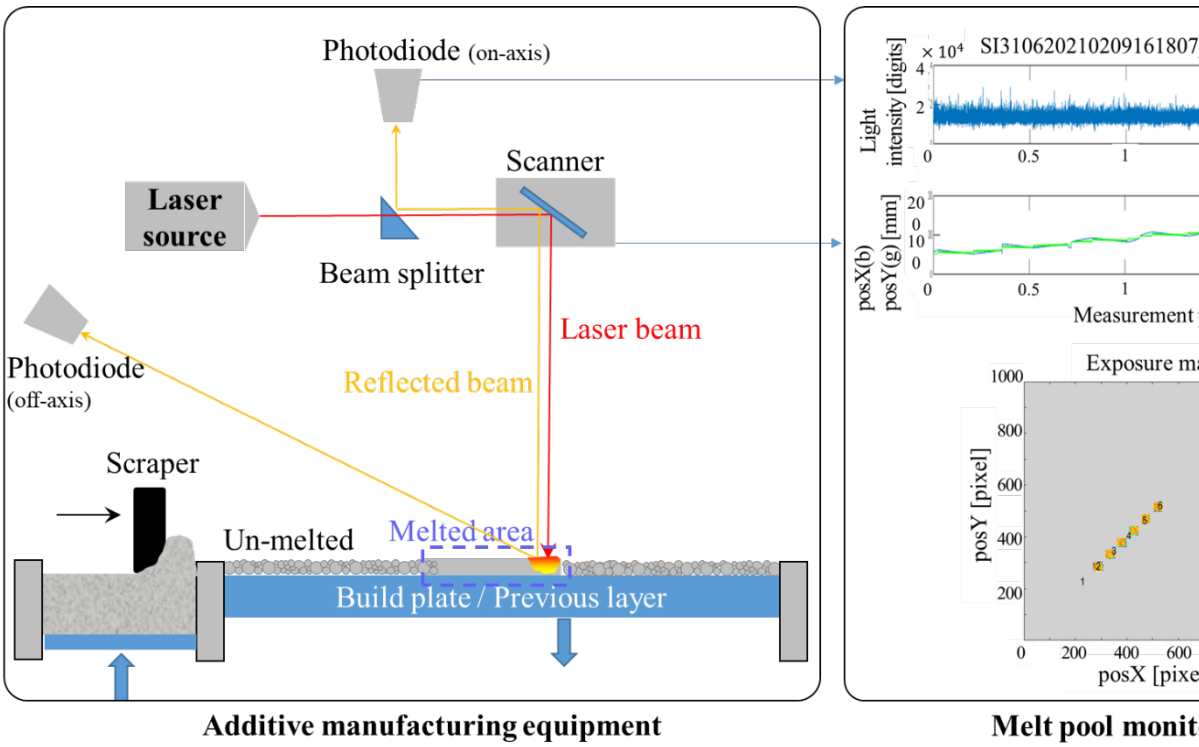

Figure 1. Schematic diagram of the L-PBF process (especially in EOS system)

2.1.3. Computed tomography (CT) analysis

In general, computed tomography (CT) imaging is used to analyze internal defects of parts manufactured by the additive process. This non-destructive inspection method transmits adjusted X-rays according to the material, density, size, and shape of the part and reconstructs the internal image in three dimensions based on the transmittance and absorption rate. This method has the advantage of inspecting the inside without destroying the product, but for parts manufactured by the metal additive manufacturing process, it takes much time to scan, and the inspection cost is high. Therefore, if an algorithm for detecting defects based on specific data related to CT scans is developed, time and cost can be reduced [2, 13].

As shown in Figure 2, the CT imaging equipment used in the experiment consists of an X-ray source, a scintillator, and a detector. X-rays have transmitted the objects installed inside the chamber from the X-ray source according to the intensity and exposure time. It can be accelerated from 30kV to a maximum voltage of 160kV, and the transmitted X-rays are detected by a detector with an enlarged intensity depending on a lens with a magnification of 0.4x to 4x. By

rotating the target 360° (−180° to 180°), the transmittance and absorption rates in each direction are comprehensively calculated and finally stored as per-pixel data. The user obtains the final result by adjusting parameters such as voltage and magnification according to the purpose of the analysis. For the setting value in this experiment, see Section 3.3

.

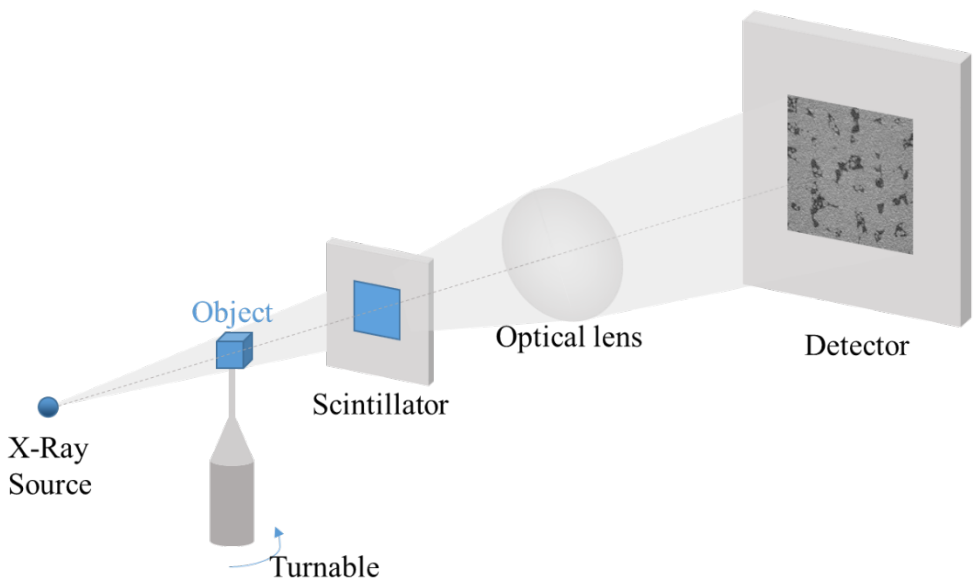

Figure 2. Schematic diagram of micro-CT

2.1.4. Convolutional neural network

The convolutional neural network (CNN) is a multi-layer feedforward deep neural network used to analyze visual image data. It is a method of expressing a high-dimensional image through a low-dimensional pattern by utilizing hierarchical characteristics of image data. An artificial neural network composed of only fully connected layers has a one-dimensional array as input data, whereas CNN can maintain spatial information by using a three-dimensional or four-dimensional array as an input. So CNN is mainly used for image recognition because it can prevent lower accuracy due to the lack of information and the loss of spatial information [14, 15].

As shown in Fig. 3, the structure of a general CNN consists of a combination of convolution layers and pooling layers that extract image features and classes and a connection of fully connected layers that predict values. The input image's dimension is reduced through convolution with a specific parameter called a filter, and a feature map is derived. As the data size becomes smaller by subsampling in the pooling layer, and this process is repeated, it is implied as low-dimensional data representing the characteristics of the input data. In

the final fully-connected layers, classification and regression according to the user's purpose are performed. Since the melt pool data is also 2D data obtained for each layer, it can be assumed as images, and CNN can be used to extract the features of the original data.

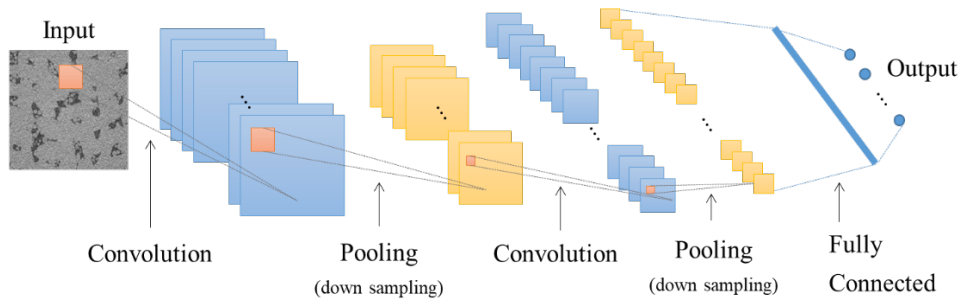

Figure 3. General CNN architecture (two-dimension)

2.2. Related research

2.2.1. Acoustic signal based defect detection

Several studies based on acoustic signals have been conducted to detect abnormalities during the process. Shevchik et al. installed a fiber bragg grating (FBG) sensor for acoustic signal collection on the

inner side wall of the additive manufacturing equipment and collected acoustic signals generated during the process through a read-out system. It was labeled with an optical microscope cross-sectional image of the specimen for supervised learning. The proposed spectral convolutional neural network (SCNN) showed 83% to 89% classification accuracy [16]. Ye et el. used acoustic signals and a deep belief network (DBN) to detect normal states, balling, and overheating defects with an accuracy of about 72% [17]. However, the method of using acoustic signals has some disadvantages. Acoustic signals have directionality, and there are numerous considerations, such as decreasing with distance and overlapping with reflected signals to generate noise. Hence, various conditions such as sensor selection, data collection location, and algorithm development for noise filters must be determined in advance, and the results vary considerably [18].

2.2.2. Image-based defect detection

Another method to evaluate the quality of parts manufactured by 3D printing is an image-based defect detection method. By installing a high-speed CCD camera in the chamber of the 3D printing equipment,

an image of the region of interest (ROI) is captured and acquired every time the modeling of each layer is finished. After acquiring image data, some studies have been conducted to process images in various ways. Luke scime et al. manually classified defects such as swelling, porosity, and misprint by the shape of anomalies that occured during the process and performed supervised learning with the CNN algorithm [19, 20]. They proposed a model that classifies defects using only images, and experimentally revealed that the multi-scale convolution neural network (Ms-CNN) has higher accuracy than other artificial intelligence models. Similarly, Gobert et al. obtained multiple images by mounting a digital-single-lens reflex (DSLR) camera. A binary classification method called support vector machine (SVM) was used to distinguish the defect from normal. For the output labeling for supervised learning, coordinates were experimentally matched through the 3D CT scan result, and the classification result showed an accuracy of 80% [21]. Another study to automatically measure the porosity of additive manufacturing through melt pool shape was conducted by Zhang et al. [22]. Although the study was limited to single tracks, using images and CNN, they predicted pores with a small

size of 100 μm or less with 91.2% accuracy.

The above studies have disadvantages in that additional equipment needs to be installed, high-performance equipment for processing image data and much time are required. In addition, since most detection is performed based on 2D images, it is not easy to consider the characteristics of the multi-layer method of PBF. So the above research were conducted focused on the detection of lack-of-fusion pores among the pore types because it is difficult to find the keyhole shape pores, which are more affected by the upper and lower layers than the lack-of-fusion in the 2D image.

3. Experimental Setup

3.1. Material and Equipment

3.1.1. Material

The material used in this experiment is Ti6Al4v grade 23 powder of EOS GmbH. According to the EOS, it is a well-known light alloy characterized by excellent mechanical properties and corrosion resistance combined with low specific weight and biocompatibility. Its material characteristics make it suitable for many high-performance applications in aerospace. Its maximum tensile strength and yield strength are 1050 MPa and 940 MPa, respectively, and it has a particle size distribution of 20um-80um. For the detailed composition of this material, see Table 1.

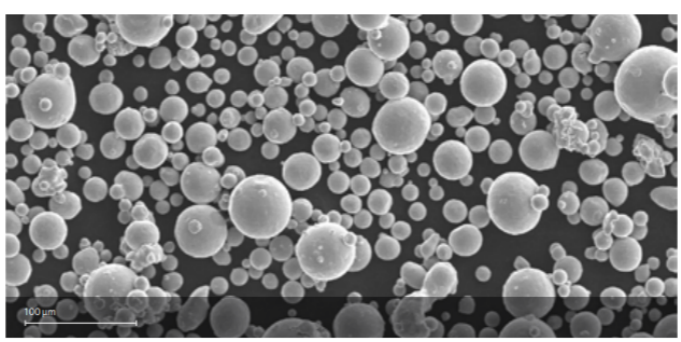

Figure 4. SEM image of Ti6Al4v grade 23 powder (from EOS

datasheet)

Table 1. Chemical composition of Ti6Al4v grade 23 powder (from EOS datasheet)

Component	Ti	Al	V	O	N	C	H	Fe	Y
Wt [%]	Balance	5.5~6.5	3.5~4.5	0.13	0.05	0.08	0.012	0.25	0.005

3.1.2. Equipment

Commercial EOS M290 L-PBF additive manufacturing equipment and the in-situ monitoring system EOSTATE Melt Pool software were adopted to fabricate the part and analyze MPM data. M290 emits a laser beam up to 400 W and 100 μm in diameter from a laser source at scan rate up to 7.0 m/s. The maximum construction volume is $250 \times 250 \times 325\ mm^3$ and when the former layers printing is finished, the orientation of the laser is rotated 67 degrees, and the last layer is radiated. The detailed specification of the equipment is shown in Table 2.

Table 2. Specification of M290 additive manufacturing system(from EOS datasheet)

Laser type	Power (Max)	Focus(Beam) diameter	Scan speed (Max)	Construction Volume	Wave length
Yb-fiber	400 [W]	100 [μm]	7.0 [m/s]	$250 \times 250 \times 325\ [mm^3]$	1060 – 1100 [nm]

Raw data can be stored and visualized by specific software, EOSTATE Meltpool Analysis Toolbox. Two photodiodes are separately mounted to collect data in real-time, except for parts for manufacturing in the M290 machine. One photodiode is arranged on the same axis as the laser input path (on-axis) and the other is set in a fixed position (off-axis) to capture light emission from the melt pool. As shown in Figure 1, on-axis data is measured by a photodiode through a semi-transparent mirror, spectral filter, and f-theta lens for visible and infrared light generated from the melt pool. On the other hand, off-axis data is gathered directly without any other filters. Since on-axis data is better to represent signal variation, in this paper, only on-axis data are used to avoid duplication and to utilize significant fluctuation [8].

3.2. Design of specimen with pores

In order to use artificial intelligence to detect pores, sufficient MPM data obtained under various process conditions is required. The typical defects generated in the L-PBF process are the pores caused

by lack-of-fusion (LOF) and keyhole (KH), specimens were fabricated containing that two types of pore and normal state (NS).

Based on the process parameters recommended by manufacturer of equipment and materials, the typical LOF and KH process parameters are set considering the energy density equation (Eq. (1)). It is because energy density is a standard design parameter that adjusts energy input [23]. The energy density is calculated as [24]

$$\mathrm{E} = \frac{P}{V \times H \times L} \tag{1}$$

where E is the energy density; P is the laser power; V is the scan speed; H is the hatch distance; and L is the layer thickness. Among these variables, only laser power and scan speed were varied, hatch distance and layer thickness were fixed as default values.

The overall shape of the specimen is a $10 \times 10 \times 10\ \mathrm{mm}^3$ cube. And then small abnormal process area (also cube shape) with each side of 300, 500, 1000, 1200, 1500 $\mu\mathrm{m}$ is arranged layer by layer. In order to investigate the effect on porosity according to the size of the abnormal process region, five sizes were considered, and a total of 125 small cubes were placed. For convenience, the entire specimen is divided into five domains (C300, C500, C1000, C1200, and C1500)

virtually. C1500 means an area including 25 abnormal process areas of $1500 \times 1500 \times 1500\ \mu m^3$. And the y-direction distance between the edge of abnormal process regions is set to be at least 500 μm, considering the upper layer's thermal effect to previous layer and the melt pool depth experimentally observed in similar scan parameters [25, 26]. Except for abnormal process areas, the other regions were set with normal process parameters (EOS standard). The detailed shape of specimens is shown in Figure 5.

Considering the specification of the equipment and the properties of the material, six process parameters were determined. According to the energy density equation and variables, three LOF (L1, L2, L3) and three KH (K1, K2, K3) process parameters were selected. Specimen with normal process parameters are not manufactured separately because they were printed outside the abnormal process area. Also, all the specimens are printed only inskin area without contour. These parameters are described in Table 3. Specimens are treated in a separate vacuum chamber for two hours to release residual stress, and hot isostatic press (HIP) is not performed because of the possibility that internal pores will be removed.

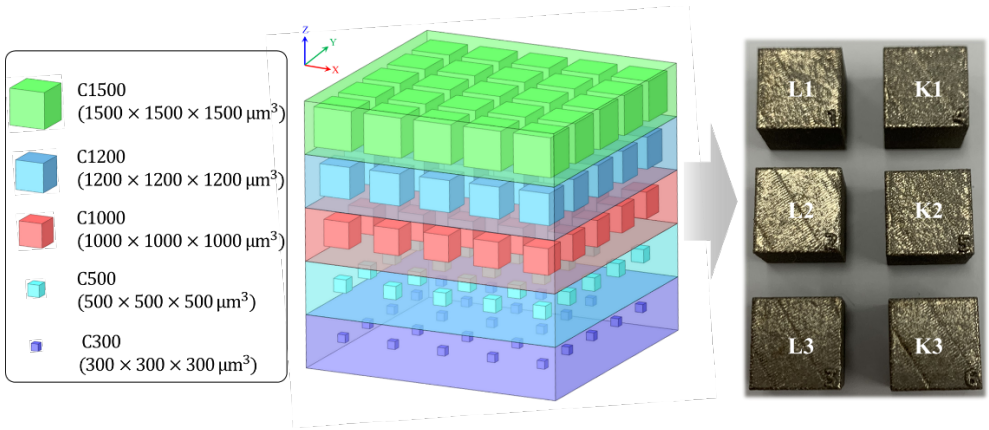

Figure 5. Design of the specimens with abnormal process region (left) and real printed specimens (right)

Table 3. Process parameters of each specimen

No.	Power [W]	Scan speed [mm/s]	Hatch distance [μm]	Layer thickness [μm]	Energy density $[J/mm^3]$
Ref.(standard)	280	1200	140	30	55.56
L1	100	1200	140 (fixed)	30 (fixed)	19.84
L2	200	1600			29.76
L3	200	1200			39.68
K1	310	1200			61.51
K2	370	1000			88.10
K3	370	800			110.12

3.3. Porosity analysis with X-ray microscopes

Micro-CT, a non-destructive inspection, is conducted to analyze the location and size of internal pores. The equipment used in CT scan is Xradia 620 versa (Carl Zeiss USA), and the detailed settings of the scan are shown in Table 4. Since the specimen is a titanium metal, the voltage is set to the maximum of 160 kV, and the exposure time is also set to be relatively long at 2.5 s. In addition, not part but entire cubic regions need to be scanned; an 0.4x optical lens and HE3 filter are used. The 3D reconstruction of the CT data is performed with Dragonfly software of ORS Inc., linked with CT equipment. Reconstructed data files (file format .txm) are segmented with another image processing software, Geodict of Math2Market GmbH. The software can align and rotate the images easily, and since the workflow can be saved, allowing the same operation on six specimens. Figure 6 and 7 shows the cross-sectional binary images at 0.6 mm height from the top of six specimens and segmentation results in three dimensions. These CT data is then used for building training and validation dataset, analyzing the distribution of pores. Results will be described in Chapter 5.

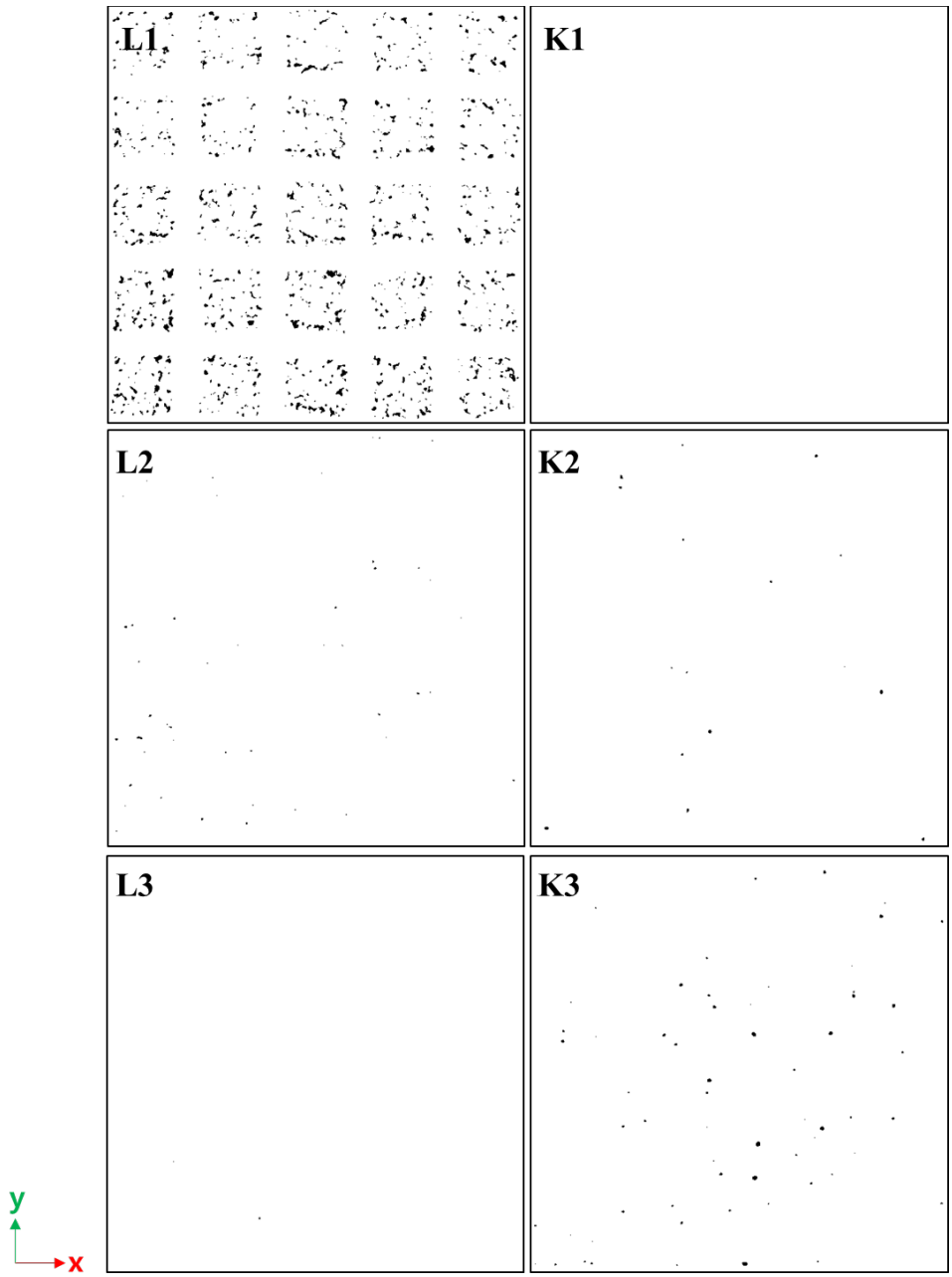

Figure 6. Binary cross-section images of each specimen (at the 0.6 mm height from the top layer)

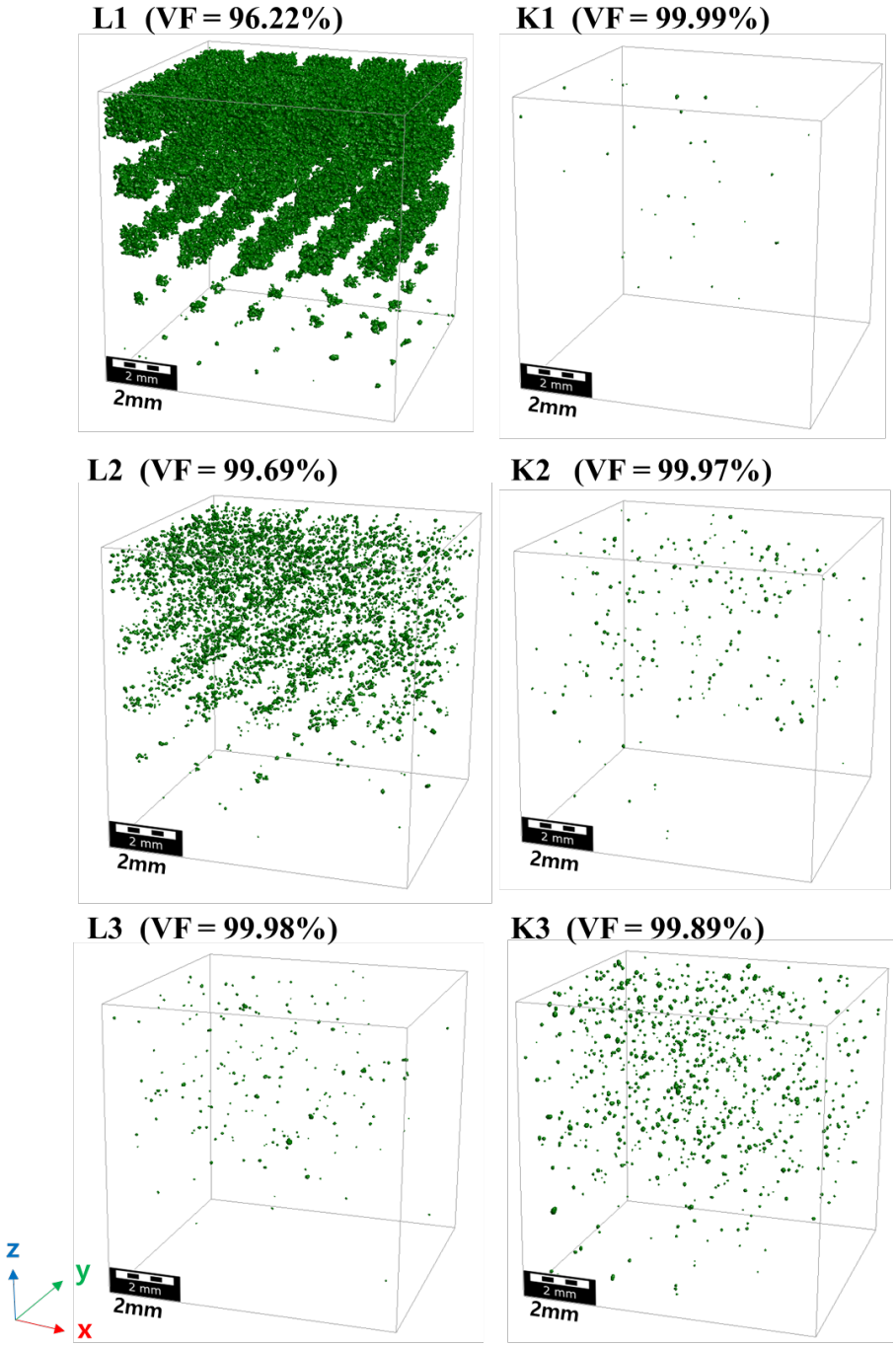

Figure 7. Segmented specimens with pores (green) and normal part

(white)

Table 4. The setting value of the micro-CT equipment

Voltage	Current	Exposure time	Optical lens	Filter	Pixel size
160 kV	154 mA	2.5 s	0.4x	HE3	15 μm

3.4. Melt pool monitoring data preparation

In order to extract MPM data from additive manufacturing instruments, EOSTATE Meltpool (additional equipment) described in Section 2.1 and Analysis Toolbox software for data presentation are required. Because the equipment manufacturer blocked access to the original MPM data to prevent re-producing, additional macro software is used to extract raw data. All the result files created in Meltpool Analysis Toolbox software are saved as MATLAB figure files (file format .fig), and then raw data is extracted in the form of a matrix consisting of x, y, and z positions and laser intensity using the separate MATLAB code.

3.4.1. Preprocessing of MPM data

Since the MPM data is collected at 60,000 Hz frequency, the location of the data point depends on the scan speed, which is the process parameter. Because the scan speed of the normal and abnormal regions is different within a single specimen, the interval of data points is different. Moreover, since the MPM data is a group of scattered points having sparsity, they must be transformed into a suitable form.

In this study, data are preprocessed using inverse distance weighted interpolation function with radial basis function as the nodal functions [27], which assigns weights according to the distances of points included in the radial range to consider nearby data effectively to improve computational efficiency. For the given point $\mathbf{x} = \{x, y, z\}$ in three-dimensional space, given the dataset $\mathbf{X} = \{\mathbf{x}_1, \mathbf{x}_2, \mathbf{x}_3, \ldots, \mathbf{x}_n\}$, and the corresponding function values f_i, $(i = 1, 2, 3, \ldots, N)$, interpolant $F(\mathbf{x})$ is defined as

$$F(\mathbf{x}) = \sum_{i=1}^{n} W_i(\mathbf{x}) Q_i(\mathbf{x}) \tag{2}$$

where $Q_i(\mathbf{x})$ is nodal function which satisfied $Q_i(\mathbf{x}_\mathrm{i}) = f_i$, and $W_i(\mathbf{x})$ is weight function defined as

$$W_i(\mathbf{x}) = \frac{Z_i(\mathbf{x})}{\sum_{k=1}^{n} Z_k(\mathbf{x})} \tag{3}$$

Where

$$Z_i(\mathbf{x}) = \left\{ \frac{[R - D_i(\mathbf{x})]_+}{R D_i(\mathbf{x})} \right\}^2 \tag{4}$$

For

$$[R - D_i(\mathbf{x})]_+ = \begin{cases} R - D_i(\mathbf{x}) & (D_i(\mathbf{x}) < R) \\ 0 & (D_i(\mathbf{x}) \geq R) \end{cases} \tag{5}$$

where R is radius of influence (20 μm in this study), $D_i(\mathbf{x})$ is Euclidean distance between $\mathbf{x}$ and $\mathbf{x}_\mathrm{i}$ ($D_i(\mathbf{x}) = \| \mathbf{x} - \mathbf{x}_\mathrm{i} \|_2$). $Q_i(\mathbf{x})$ is the function of radial basis function φ [27] and defined as follows

$$Q_i(\mathbf{x}) = \sum_{j=1}^{n_q} c_j^i \varphi(\| \mathbf{x} - \mathbf{x}_\mathrm{j}^\mathrm{i} \|_2) \tag{6}$$

And

$$\varphi(r) = (1 - r^6)_+(35r^2 + 18r + 3) \tag{7}$$

where n_q is the number of neighbor points of $\mathbf{x}_i$; c_j^i is the coefficient for solving the linear equations.

This process is performed within the bounding box of a cubic shape, considering that MPM data were measured in 3D space. It is because the extracted data is a matrix of laser intensities according to x, y, and z positions. Since the size distribution of pores generated in the specimen is generally less than 100 μm, the bounding box volume is sufficiently set to be large as $300 \times 300 \times 300\ \mu m^3$ [28]. Then the interpolated data is transformed into a $30 \times 30 \times 30$ voxel grid and used as an input value for the CNN model. This 3D moving window represents a local characteristic, so it is necessary to scan the entire MPM data to evaluate the whole part. With this moving window, local inspections are repeated at intervals of 150 μm sequentially. The the interval length is designated as half of the window size to avoid missing pores at the edge of the window. The schematic of this procedure is shown in Figure 8.

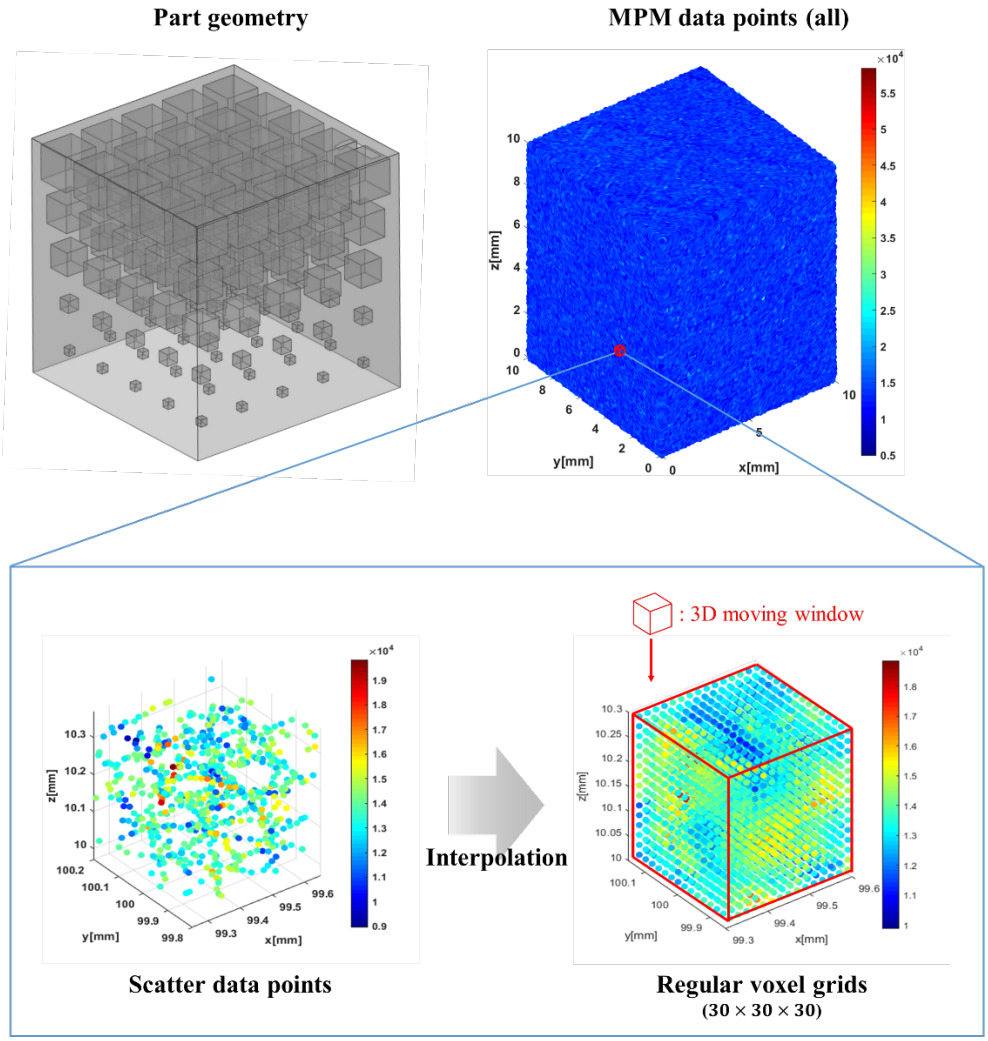

Figure 8. Interpolation process from scattering data points to regular voxel grids

3.4.2. Training and validation dataset labeling

The data to be used in the 3D-CNN network proposed in this paper should be labeled with the output value according to the input value (input-output pair) for supervised learning. In addition, a sufficiently large amount of data is required to increase the efficiency of learning and make the results accurate. Since the location of pretended pores and abnormal process parameters in samples are predefined, the interpolated MPM data at each specimens L1, L2, L3, K1, K2, and K3 can be easily labeled with the corresponding micro-CT data.

If the local void volume fraction within the bounding box is more than 1% (equal to the cubic volume of 0.00027 mm^3 and spherical pores with a diameter of about 80 μm), the corresponding interpolated MPM data is treated abnormal state. Except for such cases, all are considered as normal state (NS). Moreover, if the abnormal state is found in the LOF specimens (L1, L2, and L3) and KH specimens (K1, K2, and K3), the interpolated MPM data in the bounding box is labeled LOF and KH, respectively. Then, this procedure is repeated sufficiently many times on the different positions to build the training

dataset.

Each input-output pair of LOF, KH, and NS categories is illustrated in Figure 9. As shown in the color bar of the interpolated data figure (top row), LOF has a low light intensity of about 6000 to 16000, and this means not enough energy is supplied to the powder melting. As a result, corresponding CT data shows a large spherical or unspecified shape of pores [28-30]. On the contrary, KH has a relatively high light intensity about 13000 to 27000. It also causes spherical pores, but these are affected by the over-melting of the powder resulting from the high energy input [6, 29, 31]. In the case of NS with a light intensity about 15000, pores are not formed with a voxel size of 15 μm for setting of micro-CT. The local volume fraction of solid (V_l) for each case is calculated and labeled by quantifying the part of solid voxels (shown as white) in the bounding box.

After the data interpolation and labeling procedure, the dataset, which has 30000 samples, is prepared for CNN training. The dataset consists of 18000 samples from LOF and KH class (9000 samples each) and 12000 samples from NS class. In addition, 12000 samples for the NS class are extracted from the normal process region of LOF and KH

specimens in 5:5 ratios to equally consider high and low energy conditions.

Table 5. Training dataset composition

Class	LOF	KH	NS
Number of samples	9000	9000	12000 (6000+ 6000)

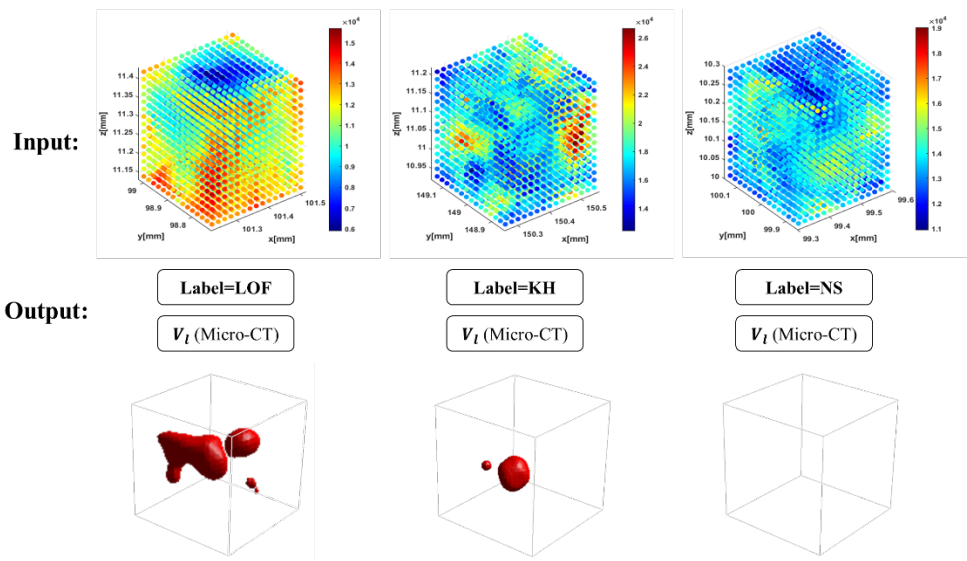

Figure 9. Input-output pair of each category (LOF, KH, NS) for 3D-CNN training

4. Pore Detection Method

Since the L-PBF method of additive manufacturing is a layer-by-layer process, it is impossible to determine defects directly in 2D MPM data of a specific layer. The upper layer affects the previous layer, and the cause of pore formation is light intensity and various factors such as gas flow. Hence, a method of applying CNN to learn the features of image datasets in various applications is used in three-dimensional space. The advantage of this 3D-CNN is that it can automatically extract optimized feature information through multiple convolution and pooling layers unlike conventional fully connected artificial intelligence network. By performing convolution calculations using training data, weights can be obtained to minimize the loss function, and results can be predicted at a low computational cost by calculating the weights with unlabeled data.

4.1. 3D-CNN model for pore detection

The 3D-CNN model proposed in this study is shown in Figure 10. This model uses interpolated local MPM data, transformed with 30×30×30 voxel dimension (Section 3.4.1), as the input. The input data

is scanned with a 3D kernel of convolution layer for performing convolution calculation. In this model, kernel size is set to $3 \times 3 \times 3$ and stride is 1. Each kernel has its weights and biases, which have to be trained to extract feature maps of the input. After the convolution computation, as the activation function, rectified linear unit (ReLU) is used to prevent gradient vanishing problem that appears as the depth of the network increases [32]. Besides ReLU, a few activation functions have been used in the neural network including sigmoid and hyperbolic tangent function in other studies. However, ReLU is the most popular method and fast for most of the cases, because when the input value is less than or equal to 0, the output value is treated as 0. The feature maps extracted from the convolution layer then flow into the pooling layer that reduces its dimensions according to certain conditions. Among the pooling method, max pooling operation with a kernel size of $2 \times 2 \times 2$, which leaves only maximum value in the pooling kernel, is selected. After the convolution-pooling operation is repeated twice, the extracted feature maps are converted into a one-dimensional structure in the flatten layer, which is connected to the fully connected layer. The three output neurons of the final layer are

used for pore classification (LOF/KH/NS) through the SoftMax activation function that normalizes all inputs to value between 0 and 1 as outputs. The function can be written as

$$p_{i,j} = \frac{\exp(a_j)}{\sum_{i=1}^{3} \exp(a_k)} \quad (j = 1,2,3) \tag{8}$$

where a_j is the value at each neuron, and $p_{i,j}$ is the predicted probability that the ith sample is classified to the jth class. As can be seen in the equation, the sum of the output values becomes 1. It means the probability that the output value can be classified into a three classes. The remaining one neuron is used for predicting the volume fraction, and since two-purpose CNNs are combined, the computational cost is not wasted due to duplication, and both can be efficiently learned.

Also, the joint objective function is defined as follows to perform both classification and regression. An equation such that the sum of the losses of the two functions is minimized is

$$\operatorname{argmin} w_c L_c + w_r L_r$$

w stands for weight and L means determined loss function by the purpose. Subscript c and r denote classification and regression, respectively. In this paper, the most widely used functions categorical

cross-entropy error (CEE) and mean square error (MSE). Since CEE is the activation function for classification, input values are $p_{i,j}$, so L_c can be computed as

$$L_c = -\frac{1}{N}\sum_{i=1}^{N}\sum_{j=1}^{3} t_{i,j}\log\left(p_{i,j}\right)$$

where N is the number of samples, and $t_{i,j}$ is the ground truth for classification between 0 and 1. And L_r, which is the mean square error, can be computed as

$$L_r = \frac{1}{N}\sum_{i=1}^{N}(y_i - t_i)^2$$

where y_i is the predicted value, and t_i is ground truth for regression. The overall 3D-CNN is trained using Adam optimizer with a 0.0005 learning rate.

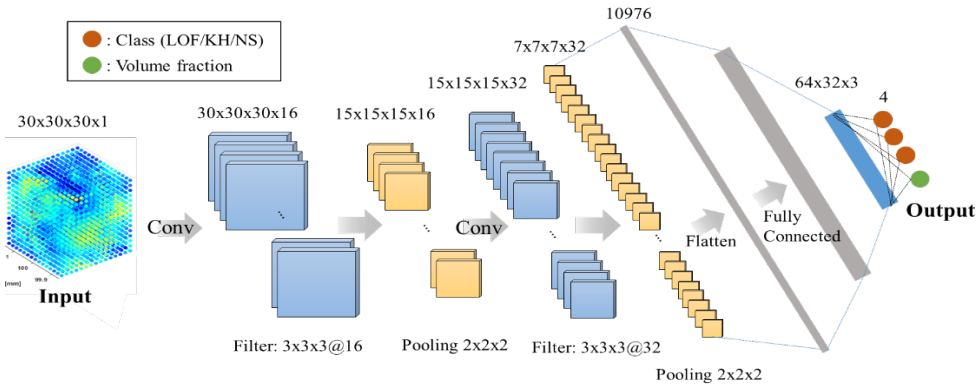

Figure 10. The combined 3D-CNN model architecture for

classification (pore detection) and regression (volume fraction prediction)

4.2. The decision of hyperparameters for 3D-CNN

The hyperparameters of the CNN model, such as kernel size, stride, padding, and number of neurons, are variables to be specified by the user. Moreover, they depend on the type or size of the data and the difficulty of the problem. Overfitting may occur if these are not properly set, appropriate hyperparameters should be set and verified through data. For the above reasons, various sets of hyperparameters are considered and tested using the mean squared error (MSE) and classification accuracy. The form of the model is divided into five types according to the network structure (number of layers and neurons), and is evaluated once more according to the loss weight ratio. Except for configuration 4, zero padding is applied to the convolution calculations to prevent loss of spatial information.

To evaluate each model, 20% of the entire training dataset is used, and training data and validation data were divided 8:2. Table 6 shows the results of the evaluation with each hyperparameter. In the table, Conv(a,b) means convolution layer with the number of kernels

(a) and the size of the kernel (b), and FC(a×b) means fully connected layer with the number of neurons. In comparing configurations 1 and 2 or 4 and 5, the error tends to decrease, but the depth of the network is not significantly related to the improvement in accuracy. Also, as seen in 2 and 4, increasing the number of neurons of fully connected layer is positive in terms of both accuracy and error. However, the number of kernels in the convolutional layer (configuration 1 and 5) is irrelevant in terms of accuracy. Compared to 3, configuration 2 shows high accuracy and low error, so it can be inferred that zero padding is worth improving the model performance. Considering the results comprehensively, the 3D-CNN model is determined with hyperparameters of configuration two and a loss weight of 1:2.

Table 6. Performance evaluation results according to hyperparameters.

	Configuration	Performance	$w_c : w_r$		
			2:1	1:1	1:2
1	Conv(16,3)+ Conv(32,3) + Conv(32,3)+ FC(64×32)	Classification accuracy [%]	98.32	98.55	98.57
		MSE $[\times 10^{-4}]$	3.44	3.35	5.06
2	Conv(16,3)+ Conv(32,3) + FC(64×32)	Classification accuracy [%]	99.20	99.67	99.47
		MSE $[\times 10^{-4}]$	3.83	4.19	1.67
3	Conv(16,3)+ Conv(32,3) + FC(64×32) without padding	Classification accuracy [%]	98.46	98.73	99.02
		MSE $[\times 10^{-4}]$	6.43	6.27	6.20
4	Conv(16,3)+ Conv(32,3) + FC(32× 16)	Classification accuracy [%]	96.22	96.95	95.99

5	Conv(16,3)+ Conv(16,3) + Conv(16,3)+ FC(64×32)	MSE [$\times 10^{-4}$]	6.90	6.26	7.61
		Classification accuracy [%]	98.84	97.59	98.82
		MSE [$\times 10^{-4}$]	4.96	6.65	5.45

5. Results and discussion

5.1. The pore distribution of specimen

The results of measuring the specimen's total volume fraction using micro-CT are summarized in Table 7 with its abnormal process parameters. The volume fraction (V_f) of the solid increased from L1 to L3 and from K3 to K1. In terms of energy density, the closer the energy density to the normal state 55.56 J/mm^3, the higher the volume fraction. In the case of L1 and L2, a significant number of Lack-of-fusion pores are observed because they were manufactured with a lower energy density than the normal energy density. On the contrary, keyhole pores are created in K2 and K3 specimens since they had relatively higher energy density than normal. Although pores are observed in the L3 and K1 specimens, which are relatively close to the normal energy density, the volume fraction is very high compared to other specimens. It is worth noting that LOF and KH pores are intensively formed in the part set as the abnormal process region rather than the normal. Since the domain sizes of the abnormal process area are arranged differently in five (C300, C500, C1000, C1200, and

C1500), the characteristics of pores can be analyzed according to the size of each domain. Figure 11, 12 represents the pore distribution in diameter for each domain and specimen. Although the pores are actually formed in an irregular shape, they are calculated by approximating them to a spherical shape to facilitate comparison.

In the L1 specimen, large pores with a diameter of 250 μm or more are observed in L1-C1500, C1200, C1000, and C500, but in L1-C300, most of the pore diameters are 45 μm to 240 μm. In other words, as the volume of the abnormal process region increases, the maximum pore size and the number of pores also increase. Because as the abnormal process region is wider, the low energy input cannot melt the material sufficiently, so the material remains in a powder state. However, in the actual manufacturing process, the size of the abnormal process region is not distributed as large as above, so pores larger than 250 μm are unrealistic. Also, the comparison result of C300 domains of the L1, L2, and L3 specimens shows that the size and number of pores decreased as the energy density increased closer to the normal. The average pore size in diameter of L1-C300 is 122 μm, whereas that of L2-C300 is 88 μm.

In the KH specimen with higher energy density than normal, different results are observed instead of LOF. The pore sizes observed in K3-C300 range from 64 μm to 152 μm, and the maximum pore sizes were measured to be 203 μm, 183 μm, 184 μm, and 197 μm, respectively in K3-C500, C1000, C1200, and C1500, where the abnormal process region increased. And as shown in histogram of K2, the pore distribution is 73 μm to 132 μm in K2-C300, but there is no difference in the rest (K2-C500, C1000, C12000, and C1500). These results mean the size of the pores in the KH specimen has no direct correlation with the volume of the abnormal process region, and even if high energy density is input, KH pores do not occur in the entire region. In this case, pore detection is more complicated to identify because the depth of the melt pool under the KH condition is much deeper than the LOF [33, 34]. It is another reason to evaluate keyhole pores using 3D data rather than 2D single-layer data.

Table 7. The total volume fraction of specimen with abnormal process parameter

Specimen	Total volume fraction (V_f) [%]	Process parameter		
		Laser power [W]	Scan speed [mm/s]	Energy density [J/mm³]
L1	96.223	100	1200	19.84
L2	99.692	200	1600	29.76
L3	99.989	200	1200	39.68
K1	99.998	310	1200	61.51
K2	99.986	370	1000	88.10
K3	99.937	370	800	110.12

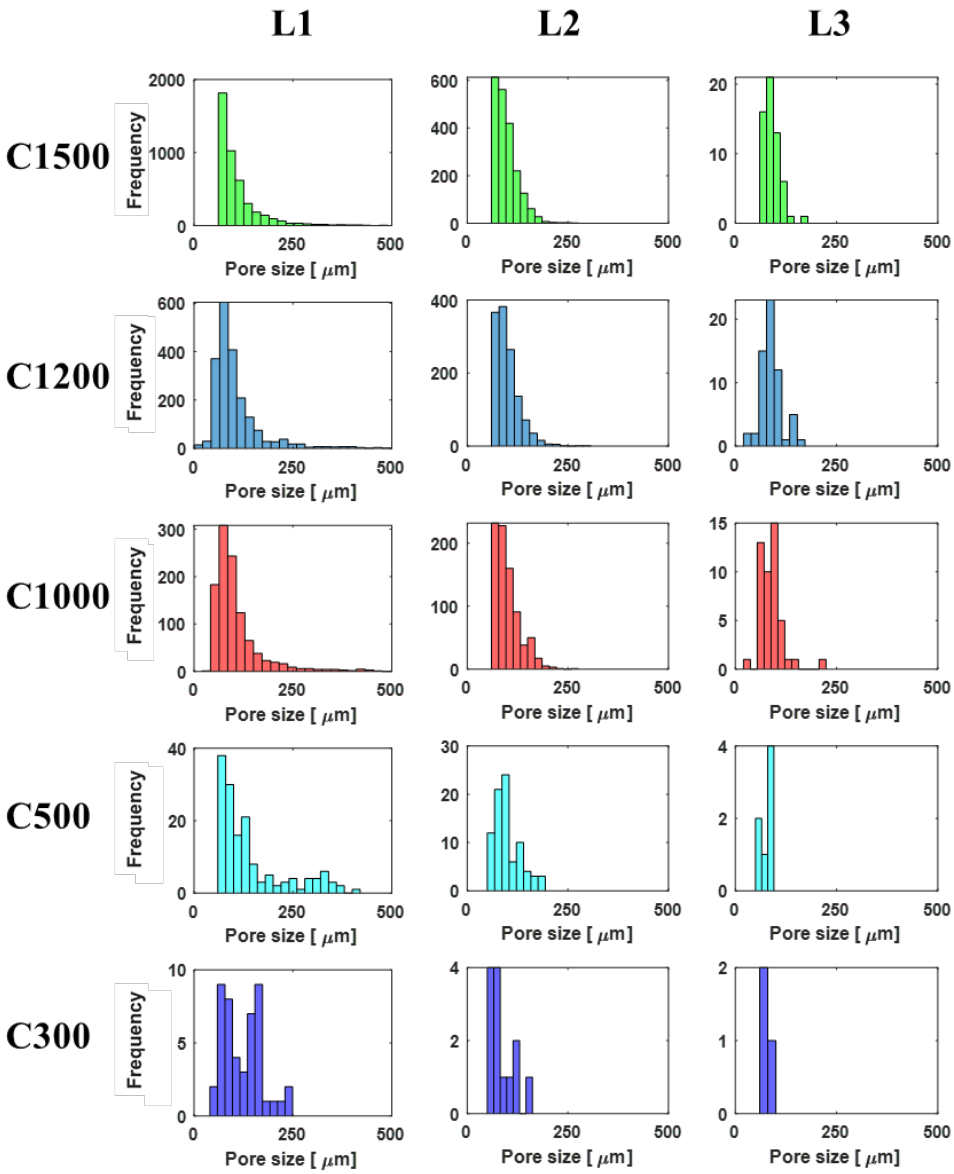

Figure 11. Pore size distribution histograms in lack-of-fusion specimens

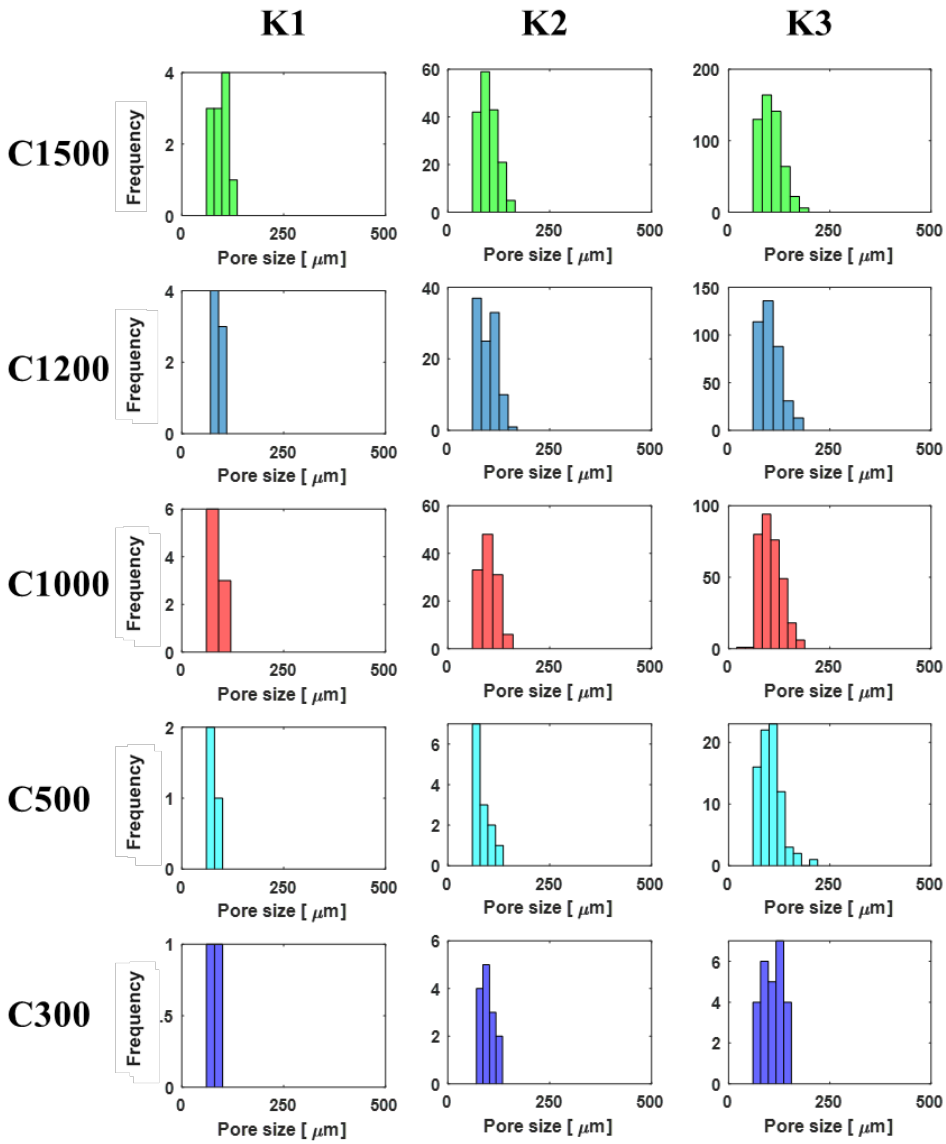

Figure 12. Pore size distribution histograms in keyhole specimens

5.2. Pore prediction results

5.2.1. Test Specimen configuration

Separate test specimens are prepared to evaluate the performance of the 3D-CNN trained in Section 4. As shown in Figure 13a, the specimen is the cubic shape of size of a $6 \times 6 \times 6\ mm^3$. An imaginary $5 \times 5 \times 5$ grid to designate the location to arrange arbitrary pores is placed into the cube. 50 locations out of a total of 125 coordinates are randomly selected, and the abnormal process area has the size of $300 \times 300 \times 300\ \mu m^3$ is placed here. It is because pores with an approximate diameter of 100 μm were formed when the size of one side of the abnormal process region is 300 μm as previously verified. Two configurations with random defect areas are considered (type I and II), and a total of four specimens are fabricated (LT1, LT2, KT1, and KT2). The process parameter sets of L1, L2, K2, and K3 are used for each specimen, and detailed information, refer to Figure 13 and Table 8. As for the test specimen, the pore size is also analyzed through micro-CT scan to confirm whether pores with a size of 100 μm were formed.

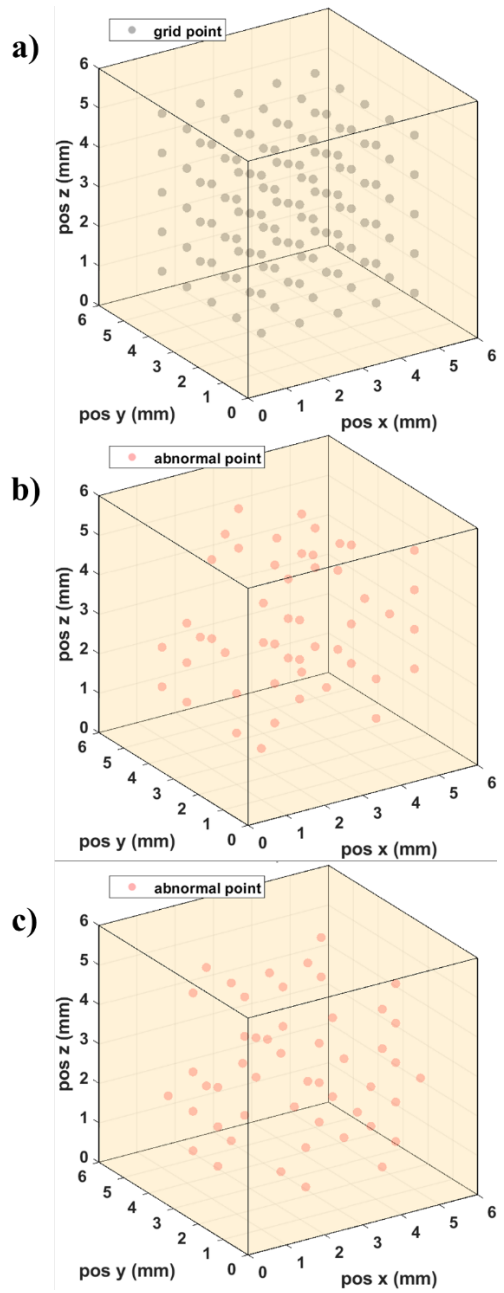

Figure 13. Shape of test specimens with random abnormal point: a) grid point (for reference); b) type Ⅰ ; c) type Ⅱ

Table 8. Process parameters and configurations for test specimens

Specimen	Configuration	Process parameter		
		Laser power [W]	Scan speed [mm/s]	Energy density [J/mm³]
LT1	Type I	100	1200	19.84
LT2	Type II	200	1600	29.76
KT1	Type I	370	1000	88.10
KT2	Type II	370	800	110.12

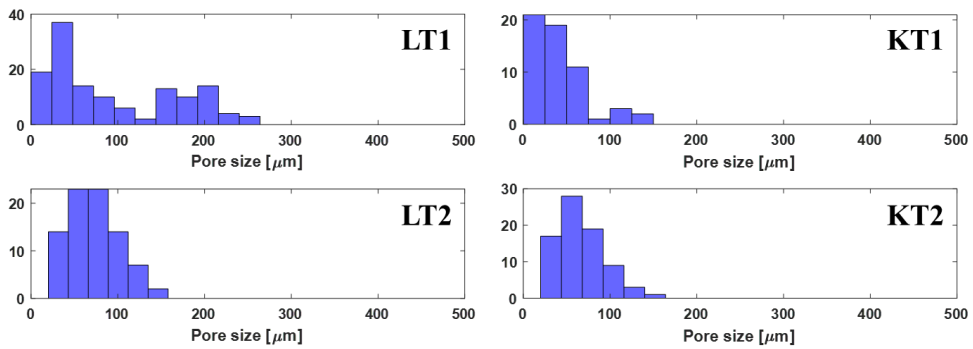

Figure 14. Pore size distribution histograms in test specimens

5.2.2. Evaluation with test dataset of test specimens

Using the interpolated MPM data extracted from the test specimen as in section 3.4, pores are predicted by trained 3D-CNN. Figure 15 and 16 show the micro-CT scan results for LT1 and LT2, respectively, and the location (a) and volume fraction (b) of the predicted pore. Although it is a specimen produced under LOF conditions, as can be seen in the figure, some KH indications are predicted. It is presumed that the KH indication appears because the unusual large fluctuations are shown in the normal process parameter area. In addition, most of the locations where the local volume fraction (V_l) is predicted to be less than 99% are predicted near the actual pore location. Similarly, the prediction results for KT1 and KT2, which are KH conditions, are shown in Figure 17 and 18. But in this case, the LOF indication is not predicted. It is the same that the predicted positions of the volume fraction of less than 99% are near the actual pores.

In order to quantify the classification accuracy of the 3D-CNN model used, true positive (TP) and true negative (TN) rates are calculated for the analysis results of four specimens. As shown in

Table 9, the highest accurate prediction of 78.37% is possible for the LT1 specimen. In the case of LT2, the result of 69.14% is lower than LT1, which means that as the energy density increases, the total amount of pores decreases, and false negatives increase. Similarly, in the case of KT1 and KT2 specimens, when the energy density differs substantially from the normal parameters (KT2), the TP ratio is 72.68%, and when the difference is slight (KT1), it shows a low value of 63.33%. It can also be seen that the closer to the normal parameters, the higher false negative values that are calculated. The true positive rate calculated from 63.33% to 78.37% seems low because the area including pores is set very small compared to the total volume. In addition, the false positive rate (actually normal but predicted to be defective) ranges from 0.12% to 0.26%. Although this seems low, but it can be regarded as a significant error when manufacturing in actual production. So, additional data in detailed process parameter sets are needed to reduce this.

The regression performance is evaluated in Table 10. It is expressed as the mean absolute error (MAE), which calculated the accuracy of the model, and the R^2 score, which indicates the degree

to which the estimated model fits the ground truth. The MAE of the total volume is lower than 0.1 in all four specimens since most of the local volume is in a normal state, and a few data is in LOF and KH conditions. In the case of local volume fraction is less than 99% (considered as LOF and KH prediction), the maximum MAE value is 2.38, and the R^2 score is calculated as 0.75-0.85. From this result, it can be seen that the prediction result of the regression model is suitable for the experimental ground truth. Similar to the experimental tendency, the predicted volume fraction of LT1 is 0.42% lower than LT2 and KT2 is 0.05% lower than KT1. Considering that LOF has a more significant number of pores than KH, it is reasonable that the difference is significant in LT1 and LT2 specimens.

An overall comparison of experiments and predictions is shown in Figure 19 with scattered points of local volume fraction and ideal ground truth (red line). The result indicates that volume fraction prediction of 3D-CNN model used in this paper is reasonable in the volume fraction range above 90%. Below 90%, the error increases, suggesting that an experiment with more detailed process parameter conditions is necessary than conducted in this experiment. The error

shown in below 90% can be improved if an additional dataset is augmented with a much low local volume fraction.

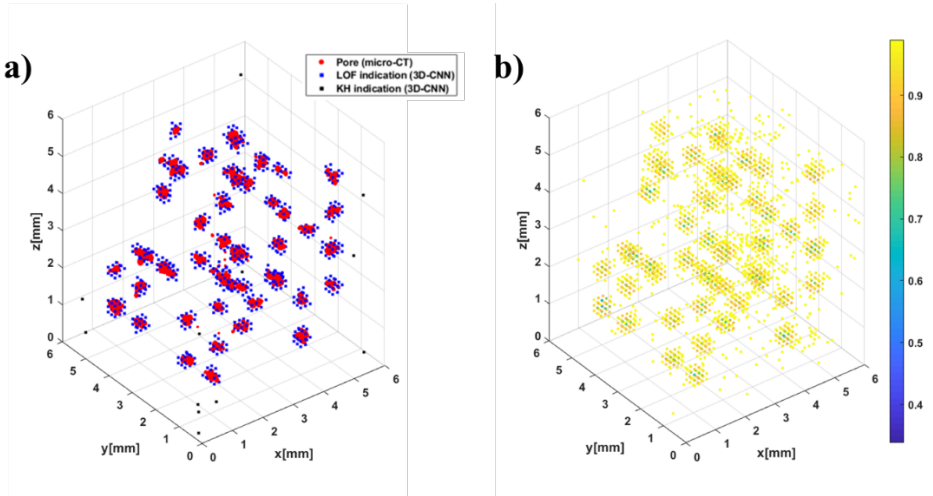

Figure 15. LT1 results: a) pore detection results compared to actual pores; b) prediction results of local volume fraction under 99%

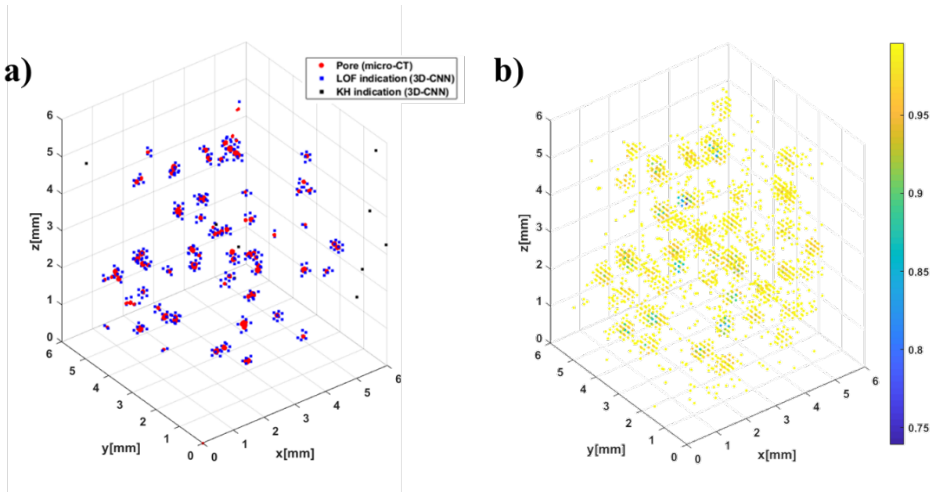

Figure 16. LT2 results: a) pore detection results compared to actual pores; b) prediction results of local volume fraction under 99%

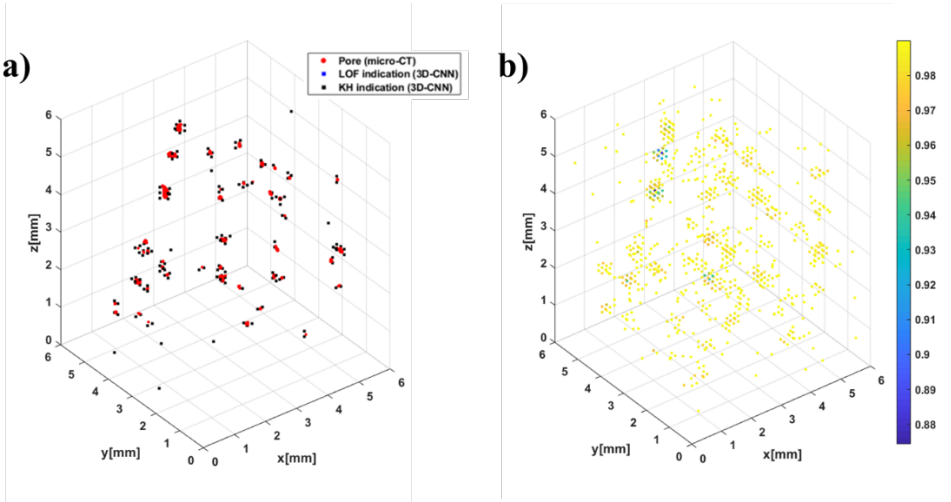

Figure 17. KT1 results: a) pore detection results compared to actual pores; b) prediction results of local volume fraction under 99%

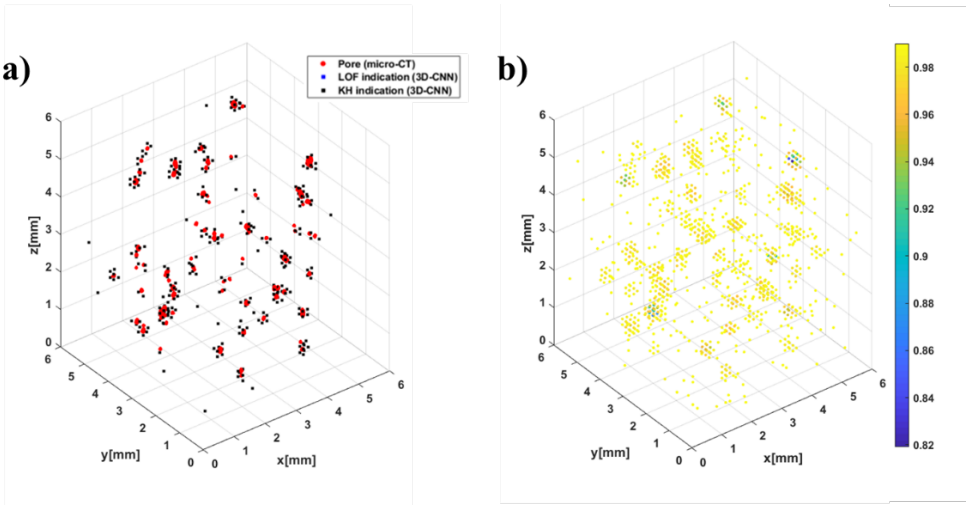

Figure 18. KT2 results: a) pore detection results compared to actual pores; b) prediction results of local volume fraction under 99%

Table 9. Classification results of 3D-CNN

Specimen	Number of counted indications			TP [%]	TN [%]
	LOF	KH	NS		
LT1	915	15	53942	78.37	99.88
LT2	378	9	54485	69.14	99.87
KT1		146	54726	63.33	99.81
KT2		302	54570	72.68	99.74

Table 10. Regression results of 3D-CNN

Specimen	MAE		R^2 score		Total volume fraction	
	total	$V_l < 99\%$	total	$V_l < 99\%$	3D-CNN	experiment
LT1	**0.0807**	**2.38**	**0.92**	**0.85**	99.48	99.84
LT2	**0.0305**	**1.25**	**0.86**	**0.79**	99.90	99.97
KT1	**0.0241**	**0.54**	**0.82**	**0.75**	99.93	99.99
KT2	**0.0476**	**0.71**	**0.87**	**0.82**	99.88	99.98

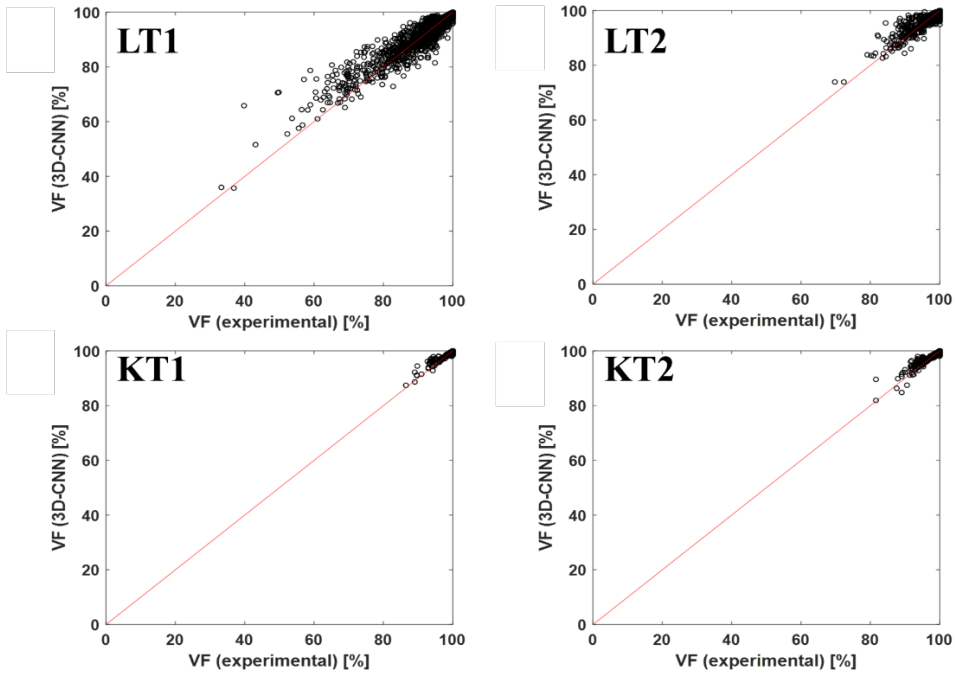

Figure 19. Comparison between predicted volume fraction with ground truth

6. Conclusion

In this thesis, the possibility of a 3D-CNN pore detection model based on MPM data, which is a cost-effective method, is studied. Experimental conditions such as process parameters, specimen shape, and defect placement are considered to extract MPM data. And then, non-uniform data are interpolated uniformly by the inverse distance weighting (IDW) method to be suitable as input for 3D-CNN. Also, micro-CT analysis is performed to analyze the distribution of pores according to experimental conditions and to specify the output value. The optimal 3D-CNN model is constructed by experimentally performing and evaluating each configuration (number of layers, hyperparameter determination, etc.). After the model is trained, the pore detection performance is verified using the test specimens containing random pores.

In the micro-CT analysis of the LOF specimen, the volume of the portion set to the abnormal energy density and the number and size of pores are clearly related, but in the case of the KH specimen, it is hardly affected by the volume. Since the mechanism formed keyhole pores so complicated, additional data and methods are needed to capture the pores generated by the keyhole process. The

detection method with 3D-CNN can detect pores larger than 80 μm diameter in both the lack of fusion and the keyhole case, in the range of 63.33% to 78.87%. Furthermore, with an R^2 score of 0.75 to 0.85, local inspection using this model can predict local volume fraction of solid less than 99%. Although this thesis focused on pore prediction, other defects such as balling and spatter, etc. can also be predicted using the proposed model by preparing a dataset with a proper experiment.

In this study, the results are obtained with some selected process parameters with limited budget and time; three additional studies are needed to improve the accuracy. First, MPM data and micro-CT analysis of samples manufactured with more diverse process parameters are required to improve accuracy. Second, a method that considers fluctuations in the original signal is needed to eliminate errors in the prediction results. Third, a combined model of classification and regression is used to prevent data duplication, but since performance differences appear depending on the weight of the loss function, it is necessary to consider a model with two separate purposes. After conducting additional research, it is expected that it will be possible to predict the quality of products more accurately without high-cost CT scans.

Reference

1. Ngo, T.D., et al., *Additive manufacturing (3D printing): A review of materials, methods, applications and challenges.* Composites Part B-Engineering, 2018. **143**: p. 172-196.
2. Thompson, A., I. Maskery, and R.K. Leach, *X-ray computed tomography for additive manufacturing: a review.* Measurement Science and Technology, 2016. **27**(7).
3. Li, J.F., L. Li, and F.H. Stott, *Thermal stresses and their implication on cracking during laser melting of ceramic materials.* Acta Materialia, 2004. **52**(14): p. 4385-4398.
4. Mercelis, P. and J.P. Kruth, *Residual stresses in selective laser sintering and selective laser melting.* Rapid Prototyping Journal, 2006. **12**(5): p. 254-265.
5. Tang, M., P.C. Pistorius, and J.L. Beuth, *Prediction of lack-of-fusion porosity for powder bed fusion.* Additive Manufacturing, 2017. **14**: p. 39-48.
6. Bayat, M., et al., *Keyhole-induced porosities in Laser-based Powder Bed Fusion (L-PBF) of Ti6Al4V: High-fidelity modelling and experimental validation.* Additive Manufacturing, 2019. **30**.
7. Kurgan, N., *Effect of porosity and density on the mechanical and microstructural properties of sintered 316L stainless steel implant materials.* Materials & Design, 2014. **55**: p. 235-241.
8. Taherkhani, K., et al., *Development of a defect-detection platform using photodiode signals collected from the melt pool of laser powder-bed fusion.* Additive Manufacturing, 2021. **46**.
9. Liu, S.Y. and Y.C. Shin, *Additive manufacturing of Ti6Al4V alloy: A review.* Materials & Design, 2019. **164**.
10. Grasso, M. and B.M. Colosimo, *Process defects and in situ monitoring methods in metal powder bed fusion: a review.* Measurement Science and Technology, 2017. **28**(4).
11. Berczeli, M. and G. Buza, *Relationship between the keyhole laser welding and the plasma - IOPscience.* 2018.
12. Abolhasani, D., et al., *Analysis of Melt-Pool Behaviors during Selective Laser Melting of AISI 304 Stainless-Steel Composites.* Metals, 2019. **9**(8).
13. du Plessis, A., et al., *X-Ray Microcomputed Tomography in Additive Manufacturing: A Review of the Current Technology and Applications.* 3d Printing and Additive Manufacturing, 2018. **5**(3): p. 227-247.
14. Gu, J.X., et al., *Recent advances in convolutional neural networks.* Pattern Recognition, 2018. **77**: p. 354-377.

15. Khan, A., et al., *A survey of the recent architectures of deep convolutional neural networks.* Artificial Intelligence Review, 2020. **53**(8): p. 5455-5516.
16. Shevchik, S.A., et al., *Acoustic emission for in situ quality monitoring in additive manufacturing using spectral convolutional neural networks.* Additive Manufacturing, 2018. **21**: p. 598-604.
17. Ye, D.S., et al., *Defect detection in selective laser melting technology by acoustic signals with deep belief networks.* International Journal of Advanced Manufacturing Technology, 2018. **96**(5-8): p. 2791-2801.
18. Hossain, M.S. and H. Taheri, *In Situ Process Monitoring for Additive Manufacturing Through Acoustic Techniques.* Journal of Materials Engineering and Performance, 2020. **29**(10): p. 6249-6262.
19. Scime, L. and J. Beuth, *A multi-scale convolutional neural network for autonomous anomaly detection and classification in a laser powder bed fusion additive manufacturing process.* Additive Manufacturing, 2018. **24**: p. 273-286.
20. Scime, L., et al., *Layer-wise anomaly detection and classification for powder bed additive manufacturing processes: A machine-agnostic algorithm for real-time pixel-wise semantic segmentation.* Additive Manufacturing, 2020. **36**.
21. Gobert, C., et al., *Application of supervised machine learning for defect detection during metallic powder bed fusion additive manufacturing using high resolution imaging.* Additive Manufacturing, 2018. **21**: p. 517-528.
22. Zhang, B., S.Y. Liu, and Y.C. Shin, *In-Process monitoring of porosity during laser additive manufacturing process.* Additive Manufacturing, 2019. **28**: p. 497-505.
23. Bertoli, U.S., et al., *On the limitations of Volumetric Energy Density as a design parameter for Selective Laser Melting.* Materials & Design, 2017. **113**: p. 331-340.
24. H. Gong, K.R., H. Gu, T. Starr, B. Stucker, *Analysis of defect generation in Ti-6Al-4V parts made using powder bed fusion additive manufacturing processes.* Additive manufacturing, 2014.
25. Ning, J.Q., et al., *Analytical Thermal Modeling of Metal Additive Manufacturing by Heat Sink Solution.* Materials, 2019. **12**(16).
26. Paul, R., S. Anand, and F. Gerner, *Effect of Thermal Deformation on Part Errors in Metal Powder Based Additive Manufacturing Processes.* Journal of Manufacturing Science and Engineering-Transactions of the Asme, 2014. **136**(3).
27. Lazzaro, D. and L.B. Montefusco, *Radial basis functions for the multivariate interpolation of large scattered data sets.* Journal of Computational and Applied Mathematics, 2002. **140**(1-2): p. 521-536.

28. Zhang, B., Y.T. Li, and Q. Bai, *Defect Formation Mechanisms in Selective Laser Melting: A Review.* Chinese Journal of Mechanical Engineering, 2017. **30**(3): p. 515-527.
29. Choo, H., et al., *Effect of laser power on defect, texture, and microstructure of a laser powder bed fusion processed 316L stainless steel.* Materials & Design, 2019. **164**.
30. Coeck, S., et al., *Prediction of lack of fusion porosity in selective laser melting based on melt pool monitoring data.* Additive Manufacturing, 2019. **25**: p. 347-356.
31. King, W.E., et al., *Observation of keyhole-mode laser melting in laser powder-bed fusion additive manufacturing.* Journal of Materials Processing Technology, 2014. **214**(12): p. 2915-2925.
32. V. Nair, G.E.H., *Rectified Linear Units Improve Restricted Boltzmann Machines*, in *Proceedings of the 27th International Conference on Machine Learning*. 2010.
33. Shrestha, S., T. Starr, and K. Chou, *A Study of Keyhole Porosity in Selective Laser Melting: Single-Track Scanning With Micro-CT Analysis.* Journal of Manufacturing Science and Engineering-Transactions of the Asme, 2019. **141**(7).
34. Lee, K.H. and G.J. Yun, *A novel heat source model for analysis of melt Pool evolution in selective laser melting process.* Additive Manufacturing, 2020. **36**.

국문초록

선택적 레이저 용융 적층 제조 공정의 용융풀 데이터를 활용한 합성곱 신경망 기반 기공 감지

이 한 울
항공우주공학과
서울대학교 대학원

본 학위논문은 선택적 소결 방식의 3D 프린팅 적층공정으로 출력된 대상의 내부 기공을 탐지하는 방법에 관한 논문이다. 금속 적층제조공법은 형상이 복잡한 부품을 전통적인 제조방식 (절삭, 주조 등) 보다 비교적 쉽고 빠르게 제작할 수 있는 장점이 있지만, 연속적으로 분말을 용융-소결시켜 제작하기 때문에 그 과정에서 일어나는 다양한 메커니즘에 의해 결함이 발생할 수 있다. 이러한 이유로 부품의 품질을 보장하기 위해 X-ray를 활용한 비파괴적인 검사 방법이 주로 사용되어왔지만, 비용과 시간이 많이 소요된다는 단점이 있다. 이를 극복하고자 공정 중의 다양한 데이터 (이미지, 음파신호 등)를 인공지능과 결합한 방법들이 시도되었고 끊임없이 연구되고 있다. 본 논문에서는 부가적인 데이터 획득

장치 없이 공정 중 용융풀에서 반사된 광량 신호 데이터를 기반으로 3차원 컨볼루션 신경망 (3D-CNN) 학습을 통해 결함 (lack-of-fusion 및 keyhole 로 인해 발생하는 기공)을 예측하는 방법을 제시한다. 훈련 및 검증을 위한 데이터를 얻기 위해 공정 매개변수인 에너지밀도를 19.84 J/mm^3 에서 110.12 J/mm^3 까지 임의로 설정하여 인공적으로 기공이 형성되는 시편을 제작한다. 제안된 신경망은 공정 중 수집된 3차원화된 광량 신호를 입력으로 받아 작은 크기의 3D moving window로 스캔하여 국부적 검사를 수행하며, micro-CT 결과로 라벨링 된 출력값과 매칭되어 학습된다. 출력값으로 기공의 종류와 국소부피분율을 예측하기 위해 분류 (classification) 와 회귀 (regression) 이 동시에 계산되는 모델이 사용되었다. 훈련된 모델의 성능을 평가하기 위해 기공이 임의로 배치된 테스트용 시편이 제작되었으며, 그 결과 제안된 모델은 lack-of-fusion 및 keyhole 두가지 경우 모두에서 직경이 80 μm 이상인 기공을 최대 78.37%의 진양성률 (true positive ratio) 로 검출할 수 있었다.

Keywords : Additive Manufacturing, Selective Laser Melting, Convolutional Neural Network, Melt Pool Monitoring, Defect Detection

Student Number : 2020-26197